

Multiscale studies of nanoconfined charging dynamics in supercapacitors bridged by machine learning

Hualin Zhan¹, Richard Sandberg², Zhiyuan Xiong¹, Qinghua Liang¹, Ke Xie¹, Lianhai Zu^{1,3}, Dan Li^{1,✉}, and Jefferson Zhe Liu^{2,✉}

¹Department of Chemical Engineering, The University of Melbourne, VIC 3010, Australia; ²Department of Mechanical Engineering, The University of Melbourne, VIC 3010, Australia; ³ARC Hub for Computational Particle Technology, Department of Chemical Engineering, Monash University, VIC 3800, Australia

The energy-delivery performance of supercapacitors is fundamentally determined by the dynamics of ions confined in nanoporous materials, which has attracted intensive interest in nanoscopic research(1). Many nanoscopic understandings, including changes in in-pore ion concentration and mobility during dynamical processes, are continuously reported(2–5). However, quantitative scale-up of these nanoscopic understandings for evaluation of the macroscopic performance of supercapacitors is difficult due to the absence of links between these scales(6). Here we demonstrate that machine learning can be used to establish such links. Starting from nanoscale, we first reveal a diffusion-enhanced migration of ions in nanopores using primarily modified Poisson-Nernst-Planck model, unlike in bulk electrolyte where diffusion counteracts migration. Using machine learning, we discover a dynamically varying ionic resistance and its equation, resulting from the in-pore ion concentration change contributed by diffusion-enhanced migration. The obtained equation is used to construct a nano-circuitry model (NCM), which describes both the macroscopic performance of supercapacitors and nanometre-resolved ionic behaviour. We demonstrate that NCM can provide additional perspectives to understand cyclic voltammograms. A Faradaic-like current peak can show in non-Faradaic processes, and an asymmetric charging/discharging can occur without ion desolvation. These is because the dynamically varying resistance delivers ions effectively for storage. The demonstrated use of machine learning could extend to other ionic systems including batteries and desalination, paving the route towards rational design.

multiscale | charging dynamics | supercapacitor | nanoconfinement | machine learning | physics-based nano-circuitry model

Supercapacitors can be viewed as ionic systems which store electrical energy by adsorbing ions at electrode-electrolyte interfaces(7, 8). When nanoporous materials are used as supercapacitor electrodes to enhance the energy storage capacity(9), the interface region is extended from the exterior surface of the electrode to the interior, forming a network of interconnected nanopores. Therefore, ions must travel through this confining nanoporous network to reach the interface deep inside the electrode, in which they would intimately interact with each other and the material, exhibiting nanoscopic effects unobserved at the exterior surface such as changes in in-pore ion concentration and mobility(2, 10, 11). However, their quantitative impact on the performance of supercapacitors is unclear, in which the collective behaviour of ions is critical(6, 8). Essential aspects in supercapacitor research therefore should involve both the study of nanometre-resolved ion dynamics confined in a single or a few nanopore(s)(5, 12, 13) and translation of these insights to the entire nanoporous network in a collective and quantitative manner. As such, we would be able to evaluate the impact of nanometre-resolved ion dynamics on the overall electrical behaviour of millimetre-sized supercapacitors,

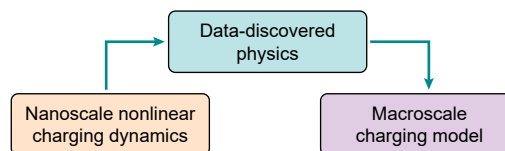


Fig. 1. Multiscale workflow for the study of nanoconfined charging dynamics. The nanoscopic findings of charging dynamics is translated to a macroscopic model through a physical relation discovered by machine learning, i.e., data-discovered physics.

e.g., predicting the macroscopic performance; and vice versa, we may capture nanoscopic insights only based on the macroscopic performance, e.g., providing additional perspectives to understand supercapacitors.

A general approach to realise this is to follow a multiscale workflow, starting from small-scale ion dynamics models and then, constructing a macroscopic model that can efficiently include the key small-scale findings/features. Examples include construction of macroscopic circuit models from either nanoscale Poisson-Nernst-Planck simulations(14, 15) or atomic-scale molecular dynamics(12), which describe charging dynamics in supercapacitors operated under simple electrical conditions. In such multiscale workflow, the results of small-scale studies are treated as inputs/variables for large-scale models(16), based on a perception that the mathematical relation of these variables can describe the nanoscopic findings. Previous studies report that conventional macroscopic circuit models which includes, for example, linear voltage-current relation of ion conduction, are able to describe the linearized charging dynamics in nanoporous materials(3, 17). However, recent studies of nanoconfined charging mechanism discover that ions could exhibit a nonlinear dynamics at non-trivial voltage(3), or produce a complicated in-pore potential(18), where existing physical relations may be difficult to account for. In addition, when compared with simple electrical condition, a commonly applied electrical condition of cyclic voltammetry (CV) can add an extra nonlinearity in the charging/discharging current when using existing physical relations in conventional circuit models(19). The unknown physical relation presents a challenge to translate these new nanoscopic findings to macroscopic circuit models. Therefore, in addition to revealing the nanoscopic insights of nanoconfined charging dynamics, another task in this multiscale study involves searching for a new physical relation to translate these insights into macroscale.

Machine learning is a field in computer science studying how to automate complex processes, such as image recognition or autonomous driving, at low cost based on data analysis(20). In addition to its recent application in physical research to

✉e-mail: dan.li1@unimelb.edu.au; zhe.liu@unimelb.edu.au

automate the design of materials/devices(21, 22) or the prediction of experiments(23, 24), it can be used to discover the underlying mathematical relation based on the analysis of simulation results(25–28). In this work, we use a machine learning algorithm to discover the equation of the unknown physical relation between the nanoscopic and macroscopic studies of nanoconfined charging dynamics, proposing a three-step strategy to complete a multiscale workflow (Fig. 1). First, in nanoscopic level, we study nanoconfined charging dynamics by investigating the interplay of ion migration, diffusion, and the effect of finite ion size (steric flux) in nanoslit-based supercapacitors primarily using a theory of modified Poisson-Nernst-Planck (mPNP)(29), under the dynamically varying electrical condition of CV. However, only ion migration can be directly correlated with the resistive relation of current and voltage in conventional circuit models(19), where diffusion, steric flux, and the time-dependent ion concentration are not accounted for. Second, we use evolutionary algorithm, a machine learning approach, to analyse the current and voltage profiles obtained by mPNP to identify their mathematical relation. Finally, we construct a circuit model which includes the discovered relation, in order to enable both bottom-up and top-down analyses of nanoconfined charging dynamics. Based on these results, we further discuss whether this approach of connecting nanoscale to macroscale by data-discovered physics can provide new perspectives to research in electrochemistry and whether it can be extended to other fields.

Nanoscopic study of nanoconfined charging dynamics. Understanding the nanoscopic mechanism of charging dynamics in nanoslit network is the first step in the multiscale workflow for supercapacitors. We study the nanoscopic charging dynamics by investigating the collective motion of ions inside nano-resolved porous structures under experimentally comparable electrical conditions, such as migration and diffusion. From the nanoscopic perspective, migration and diffusion clearly describe the transport of ions induced by separate mechanisms, i.e., electric field and concentration gradient, respectively(30–33). From the perspective of the subsequent multiscale study, the collective motion of ions interfaces directly with the macroscopic description of supercapacitors, where migration and diffusion provide transient profiles of electrical current to describe charging dynamics(3, 14, 31). In nanoslit network, we consider an additional mechanism of ion transport – steric flux – induced by the steric repulsion of ions with finite size when their concentration approaches the maximum value permitted inside nanoslits. Recently developed mPNP theory quantitatively considers the impact of migration, diffusion, and steric flux on the time-dependant behaviour of ions, allowing for straightforward analysis of charging dynamics in this work (see Methods)(29). Molecular dynamic simulation is only used as a supplementary method here. This is because, despite the accurate molecule-level description of ionic behaviour in simple nanopores, it has big gaps in time and length scales as compared with experiments, disadvantaging itself from quantitative description of collective ion flux in interconnected nanoslit networks under cyclic charging/discharging conditions (see Methods).

We carry out mPNP calculation to study the nanoscopic charging dynamics in a supercapacitor under the CV charging/discharging condition (Fig. 2a). Two identical electrodes are made of layered 2D materials with an internal struc-

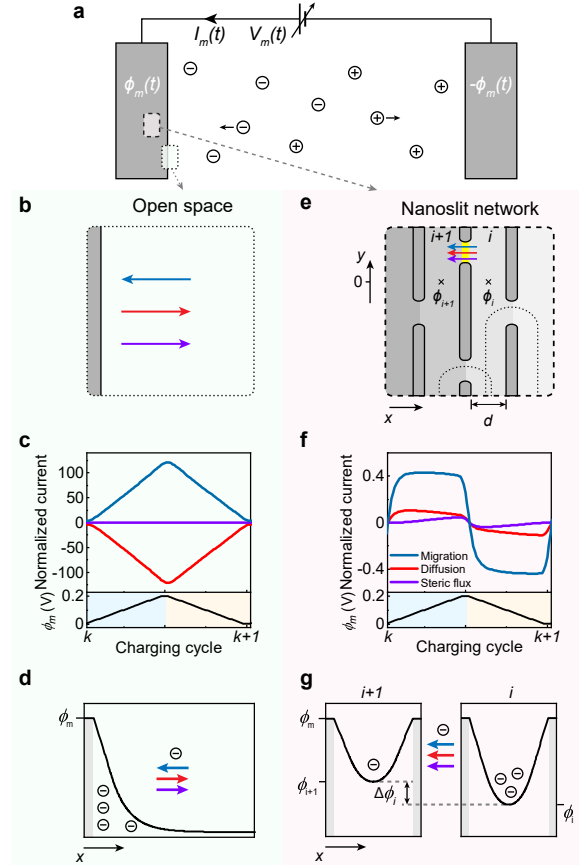


Fig. 2. Nanoscopic study: diffusion-enhanced migration in nanoslit network, as opposed to that in open space. **a**, Schematics of a supercapacitor, where the left and right electrodes have identical internal structure. $I_m(t)$ is the electric current under an externally applied voltage $V_m(t)$ is the applied voltage, which splits to equal electric potential with opposite sign applied on each electrode ($V_m = 2\phi_m$). \oplus and \ominus represent cations and anions that travel within the supercapacitor. Magnification of the dotted and dashed areas are shown in **(b)** and **(e)**, respectively. **b**, We denote the dotted region as open space. The blue, red, and violet arrows indicate the direction of ion migration, diffusion, and steric flux undercharging, as informed by mPNP calculation. **c**, Calculated ionic current contributed by migration, diffusion, and steric flux during a CV cycle, which is normalized by the maximum value of $I_m(t)$. The bottom panel shows the variation of ϕ_m during a charging (light blue region) and discharging (yellow region) process. **d**, Schematics of electric potential distribution in **(b)**. **e**, The internal structure of the membrane electrode, i.e., nanoslit network. A nanoslit (highlighted with different greyscales and indexed by i) is constructed between two neighbouring 2D materials (dark slats) in x -direction. d is the slit size. Electrical potential of i^{th} nanoslit (ϕ_i) is evaluated at the marked location ($y = 0$). The dotted curves denote the EDLs of neighbouring 2D materials, which will overlap as d decreases. **f**, **g**, Corresponding results for nanoslits, as compared with **(c)** and **(d)** for open space. The current in **(f)** is obtained across the yellow line in **(e)**, where $d = 1.5$ nm.

ture of cascading nanoslit network, resembling the typical membrane-based supercapacitors (Fig. 2e and Extended Data Fig. 1)(8, 34). We explore different slit size (d) in the range from 1.5 to 5 nm and adopt the standard KCl electrolyte of 1M concentration. On the exterior surface of the electrode (open space, Fig. 2b), our results show that the direction of migration (blue) is opposite to that of diffusion (red) and steric flux (violet) during the entire CV cycle (Fig. 2c and Extended Data Fig. 2). This is consistent with the conventional experience(35): when electric field drives ion migrating towards/away from an electrode, the increased/decreased concentration on its surface always induce a diffusion in the opposite direction (Fig. 2d).

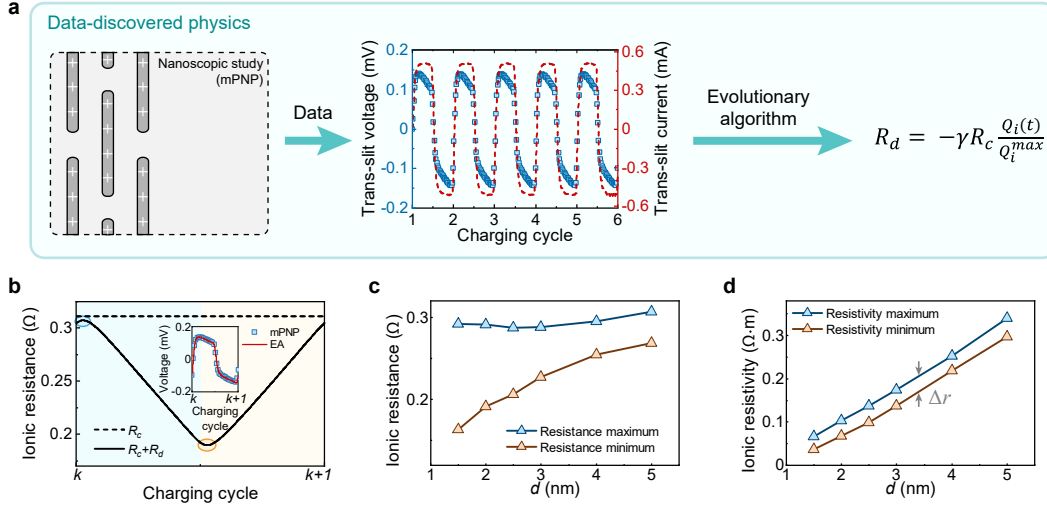


Fig. 3. Data-discovered dynamic resistance for ion dynamics in nanoslit network. **a**, Flow chart of data-discovered physics. The mPNP computational data for ion transport in nanoslit network was pre-analysed into the trans-slit voltage-time and current-time relations. They were fed to the evolutionary algorithm (EA) analysis to yield a physical constitutive relationship for a dynamic trans-slit resistance. A negative resistance component (R_d) is discovered, which depends on the net charge $Q_i(t)$ stored in the nanoslit. **b**, Variation of the dynamic trans-slit resistance $R_c + R_d$ during a CV cycle for a nanoslit network with $d = 2$ nm. The dynamic resistance reaches the maximum (circled in blue) and minimum (circled in orange) at the beginning of charging (blue region) and discharging (yellow region). Inset: $R_c + R_d$ discovered by EA (red solid line) successfully describes the trans-slit voltage shown in the middle panel of (a). **c**, The maximum and minimum values of ionic resistance as a function of the slit size (d). The slight change of the maximum resistance and the reduction of minimum resistance with the decreasing d is counterintuitive. **d**, Both the maximum and minimum ionic resistivity reduce with d , but the difference Δr changes negligibly.

In contrast, for nanoslit networks with all values of d studied, our calculation shows the same direction of migration and diffusion from the i^{th} to $(i+1)^{th}$ nanoslit in the network during the entire CV cycle, i.e., diffusion-enhanced migration (Fig. 2c and Extended Data Fig. 3). The steric flux direction also becomes the same when $d < 2$ nm. Our molecular dynamics simulations quantitatively confirm such diffusion-enhanced migration for a nanoslit network with an equivalent d of 0.59 nm (Extended Data Fig. 4 and Methods). Nanoconfinement induces a constructive interplay among all these transport mechanisms, which could be beneficial for charging dynamics in nanoporous electrodes.

The diffusion-enhanced ion migration across nanoslits in the network could attribute to the overlap of EDL under nanoconfinement (Extended Data Fig. 5a). The electrified surface attracts counter-ions to form EDL that screens the surface electrical potential ϕ_m (36, 37). For nanoslits with d smaller than twice of the Debye length (thickness of EDL), two EDLs at the two opposite surfaces overlap and form a well-shape electrical potential profile. Our analysis shows that ion transport across two potential wells in neighbouring nanoslits behaves opposite to the conventional experience in single open-space EDL. Given the i^{th} nanoslit having higher net ion charge (the difference between counter-ion and co-ion), the more efficient screening results in a lower electrical potential ϕ_i in the middle of slit than that in the $(i+1)^{th}$ nanoslit, i.e., ϕ_{i+1} (Extended Data Fig. 5b). The resultant electric potential gradient produces a migration flux of net ion charge flux from the i^{th} nanoslit to the $(i+1)^{th}$. Meanwhile, higher net ion charge concentration in i^{th} slit induces a diffusion flux in the same direction, i.e., the observed diffusion-enhanced migration phenomenon. A similar analysis can be performed for the case of a lower net ion charge density of i^{th} nanoslit to draw the same conclusion. The conventional perception that diffusion and migration flux would have opposite direction

during the charging/discharging process (in open space) cannot be transferred to the nanochannel systems in bulk nanoporous electrodes.

The anomalous diffusion-enhanced migration implies a complex nonlinear trans-slit voltage-current relation over the charging/discharging process in the nanoslit network. This inspires us to investigate the time-dependent correlation between the potential difference and ion transport across adjacent nanoslits, i.e., $\Delta\phi_i = \phi_{i+1} - \phi_i$ (trans-slit voltage) and I_i (trans-slit current). The middle panel of Fig. 3a summarises typical variations in $\Delta\phi_i$ and I_i with respect to time for the case of $d = 2$ nm. We found that this type of nonlinear voltage-current relation generally exists in all nanoslits inside the nanoslit networks with all values of d studied (Extended Data Fig. 6). It clearly cannot be described by the conventional Ohmic law with a constant resistance, and it cannot be simplified using the potential in open space(18). Establishing a physical constitutive relationship for the dynamic dependence between trans-slit voltage and current is a challenging task that is not addressed before. This constitutive relation could translate the nanoscience knowledge across length scales to macroscopic models for efficient and quantitative prediction of dynamic charging behaviour of supercapacitors.

Discover the unknown physics by machine learning to bridge multiscale studies. Evolutionary algorithm (EA), among several machine learning techniques for equation discovery including sparse regression(26) and adjoint methods(22, 27), provides a constraint-free symbolic regression method to identify mathematical expressions from provided numerical data(38). EA does not require guidance from existing knowledge to search for the global optima in a large solution space. It is therefore particularly suitable for this study since the anomalous diffusion-enhanced migration itself does not offer any mathematical guidance for searching the explicit expression of the

nonlinear trans-slit voltage-current relation. Therefore, EA is adopted here to analyse the voltage and current profiles obtained by mPNP (Fig. 3a), in order to connect the nanoscopic studies of charging dynamics with macroscopic models.

The workflow of our data-discovered physical relationship is summarised in Fig. 3a and detailed in the Methods. First, we pre-process our mPNP simulation data for trans-slit voltage and current in nanoslit networks during a charging process. Then we feed the data to EA. After evolution for thousands of generations, the relation of the voltage ($\Delta\phi_i$) and current (I_i) between the i^{th} and $(i+1)^{\text{th}}$ nanoslits in a network is identified as

$$\Delta\phi_i = I_i(R_c + R_d), \quad [1a]$$

$$R_d = -\gamma R_c \frac{Q_i(t)}{Q_i^{\text{max}}}, \quad [1b]$$

Here R_c is a positive constant resistance component. R_d is a dynamically varying resistance component and is negative for positive values of γ . $R_c + R_d$ composes the dynamic trans-slit resistance. $Q_i(t)$ is the transient net ion stored in the i^{th} nanoslit and Q_i^{max} is its maximum. γ is a fitting parameter between 0 and 1. These equations quantitatively describes the nonlinear voltage-current relation very well (inset in Fig. 3b). We analyse the trans-slit resistance in different nanoslits inside the networks with all values of d , and we note that the trans-slit voltage-current relations are surprisingly identical in the same nanoslit network (Extended Data Figs. 6 and 7). In other words, R_c and γ only depend on slit size d . The parameter γ represents the ratio of resistance reduction under nanoconfinement.

Fig. 3b shows the variation of trans-slit ionic resistance $R_c + R_d$ during a typical CV cycle for the nanoslit work with $d = 2$ nm. Slightly after the beginning of charging, $R_c + R_d$ reaches its maximum value close to R_c . Then it keeps reducing during the charging process. Slightly after the beginning of discharging, $R_c + R_d$ reaches its minimum value close to $(1 - \gamma)R_c$. In the rest of the discharging process, the resistance keeps increasing. Fig. 3c summarises the change in maximum and minimum resistance values versus the slit size d . We observe that the maximum ionic resistance remains almost unchanged when d decreases (blue triangles). This is surprising since small slit size d is expected to reduce the conductive ion numbers and increase the resistance value. Here we note that despite the reduce nanoslit size d , the interface area remains constant. Via careful analysis (Extended Data Fig. 10a), we infer that the ionic current across stacked nanoslits indeed mainly occurs at the material surface. A previous study observed short-circuit surface conduction in nanopores with continuous geometry(14), our study shows that this surface-conduction insight could be extended to stacked nanoslits due to overlapped EDL. Furthermore, we discover that the surface-conduction can be time dependent, rather than a stationary effect, as the ionic resistance reduces in the charging process. However, the minimum ionic conductance decreases with d (orange triangles in Fig. 3c), which cannot be attributed to the surface conduction alone. This urges us to analyse further the nanoconfined ion transport.

We then investigate the trans-slit resistivity, as an intrinsic property of ion transport. Both the maximum and minimum of the ionic resistivity decrease with d (Fig. 3d). This is because ion accumulation, which gives more concentrated ions in smaller nanoslits (Extended Data Fig. 7a-c), accounts for

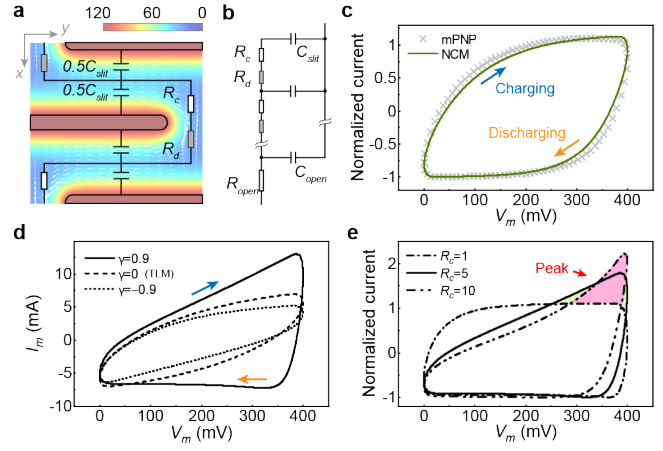


Fig. 4. Construction of a macroscopic circuit model with data-discovered dynamic resistance. **a**, Description of ion transport and storage in layered 2D material electrodes by R_c , R_d , and local capacitance of a nanoslit (C_{slit}), based on the spatial investigation of potential (colourmap) and current (white arrows) in nanoslits. Colour-scale unit: mV. **b**, Construction of Nano-Circuitry Model (NCM) to represent half-cell of a supercapacitor with the circuit elements in (a) and additional resistor (R_{open}) and capacitor (C_{open}) describing ionic behaviour in open space. **c**, CV diagram of a supercapacitor obtained NCM, which agrees well with the mPNP result. **d**, Evaluation of nanoscopic effect of confined ions on the shape of macroscopic CV diagram, where γ changes from -0.9 to 0.9. In all cases here, $R_c = 5\Omega$. **e**, Revealing nanoscopic insights from macroscopic CV diagrams: a case study of the current peak shown in the upper right corner as function of R_c , which changes from 1 to 10 Ω , rather than a result of redox reaction. In all cases here, $\gamma = 0.9$.

the decreased resistivity. The increase in ion concentration in nanoslit is delivered by migration, diffusion, and steric flux all together – diffusion enhanced migration (Extended Data Fig. 8). These electro-adsorbed ions, which are not chemically bonded with the material, can contribute to reducing the trans-slit ion resistivity. The difference between the maximum and minimum (Δr) remains nearly constant for all values of d , implying that this nanoscopic effect is not a special property only occurs in small nanoslits. Nevertheless, when taking into account the low magnitude of resistivity for small d , both the magnitude and the maximum-minimum difference of conductivity become substantial (Extended Data Fig. 9). It suggests that this nanoscopic effect, although exists in slits with all sizes studied, dominates ion transport in small nanoslits with highly overlapped EDL. Therefore, the nanoconfinement effect must be noted when constructing macroscopic models.

Building macroscopic circuit model with nanoscopic insights.

The last step in the multiscale workflow of nanoconfined charging dynamics (Fig. 1) is to construct a macroscopic model where the impact of the discovered nanoscopic effects on the overall electrochemical behaviour of the supercapacitor can be effectively evaluated. Circuit models are electrical representations of supercapacitors which can serve as such a macroscopic model for the study of charging dynamics here. They are used traditionally to interpret the macroscopic experimental results of supercapacitors(39, 40) and are being explored to predict the macroscopic performance(41, 42). Their advantages include computational efficiency of electrical response, straightforward application of voltages or currents of various forms, and direct interface between supercapacitors and external circuit loads, which allows for convenient estimation of application-specific performance(43, 44). However,

the main difficulty in using circuit models for supercapacitor research is the insufficient validation of circuit elements, resulting from the fundamental gap between the pure electrical origin of circuit models and the physio-chemical background of supercapacitors(19). Here we construct a circuit model with the definition and distribution of each circuit element being validated or correlated to the nanometre-resolved ion transport or storage, where supercapacitors can be viewed as an ensemble of nano-circuits, i.e., nano-circuitry model (NCM).

We investigate the spatial distribution of electrical potential and current in nanoslit network to allocate nanoscopic ion process at different location to each element of the NCM (Fig. 4a). Ion transport in the nanoslit network can be modelled using the data-discovered trans-slit constitutive relation ($R_c + R_d$ in equation 1) and ion storage in different nanoslit can be described by a capacitor C_{slit} , (Extended Data Fig. 10 and Methods). Our mPNP results show C_{slit} is a constant when $d > 1$ nm and remains unchanged during charging/discharging (Extended Data Fig. 11a, b). In our NCM as shown in Fig. 4b, R_{open} and C_{open} represent ion transport and storage in open space of the bulk electrolyte. For verification, we compare the computed CV diagrams by NCM and mPNP simulations in Fig. 4c for the case of supercapacitor electrode consisting of 6 layers of 2D materials with $d = 1.5$ nm ($\gamma = 0.5$). The agreement is very good. We can easily extend our NCM to larger systems including more layers (Extended Data Fig. 12) with computational cost of several minutes, whereas the mPNP simulations could take days and weeks. This is particularly beneficial for (semi-)quantitative engineering design.

CV diagrams are commonly analysed to characterize the performance of supercapacitors. They embody comprehensive information, e.g., the shape of CV curve provides an indication of the charging dynamics(41) and the enclosed area of CV curve can quantify the energy storage capacity(35). In light of its importance, here we will use NCM to evaluate the impact of the discovered nanoconfined ion dynamic effects on the macroscopic CV results of supercapacitors.

The first qualitative difference is the shape of the CV curve. We observe that the CV in Fig. 4c captures an asymmetry between charging (blue arrow) and discharging (orange arrow). For nanoslit networks with $d = 1.5$ nm, the asymmetry in CV becomes profound with the increase of layer numbers (i.e., electrode thickness) and charging rate (Extended Data Fig. 12), where more nanoconfined ions are included. Such asymmetry is not observed using the conventional transmission line model (TLM, Extended Data Figs. 11c and 12) with any parameters used (Extended Data Fig. 13a), suggesting a mechanistic difference of NCM. This can be attributed to our data-discovered dynamic resistance R_d . Fig. 4d confirms that increasing value of γ (indicator of nanoconfinement degree) change CV curves from a symmetric ellipse ($\gamma = 0$) to a trapezoid shape ($\gamma = 0.9$).

Such trapezoid CV shapes are often observed in experiments(45), particularly when ions are confined in small nanopores(46–49). Previous studies propose that desolvation of ions may lead to this asymmetry(46). We demonstrate another mechanism due to the dynamically varying trans-slit resistance under nanoconfinement. As γ increases, nanoscopic studies by NCM reveal that the reduced trans-slit resistance effectively delivers more ions to nanoslits for storage (Extended Data Fig. 14) by facilitating ion transport (Extended Data

Fig. 13b), re-emphasizing that charging process is a balance between ion storage and transport. In experiments, a large γ could be achieved by choosing small interlayer distance (d), small ion size, high electrolyte concentration, or high voltage window. Note that although a dynamically increasing resistance is not yet observed in this work, NCM can describe CV for such cases ($\gamma = -0.9$). If ion accumulation in nanoslits does not dominate the electrochemical performance, for example ions may be depleted or trapped by functional groups, a dynamically increasing resistance may occur.

The second quantitative difference is the enclosed area of CV. The area enclosed by the solid curve in Fig. 4d is clearly larger than that enclosed by the dashed curve, predicting a higher energy storage capacity for large γ (Extended Data Fig. 14). This suggests that not only the power but also the energy density of supercapacitors can be improved by facilitating ion transport, as charging process is a balance between ion storage and transport.

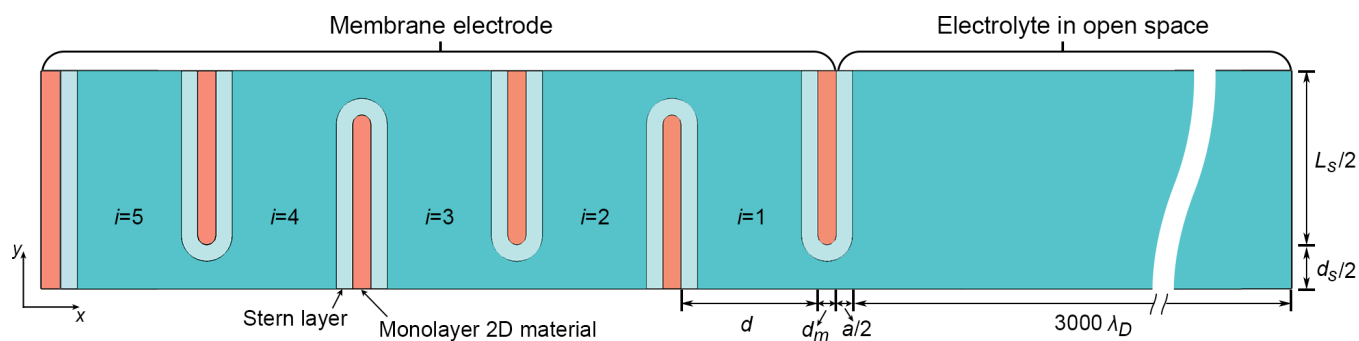
The third qualitative difference is the current peak in CV curve, which is consistently predicted by our NCM (Fig. 4e, Extended Data Fig. 12). An intuitive electrochemical analysis commonly associates current peaks in CV diagram to Faradaic processes or redox reactions(35). However, no Faradaic processes are involved here. This again could be attributed to the dynamically varying trans-slit resistance, where a substantial decrease in its magnitude requires a much higher delivering rate of ions, i.e., current, as charging proceeds. Due to the critical role of the magnitude of resistance here, rather than the ratio γ , a higher value of R_c could make the peak more evident. R_c could be increased by lowering ion mobility or electrolyte concentration. Therefore, a Faradaic-like peak in CV may not necessarily indicate a Faradaic process, providing an additional perspective for future discussion of electrochemical results. Our results may offer fresh ideas and insights to understand the macroscopic performance of supercapacitors. Meanwhile, the highly efficient computational tool of NCM lays a foundation for quantitative engineering design of realistic electrodes on multiple scales .

Conclusion. We demonstrate that machine learning can be used to identify the previously unknown mathematical relation for nanoscopic transport of nanoconfined ions, i.e., diffusion-enhanced migration, for inclusion in a macroscopic circuit model. In nanoscale, ions confined in nanoporous networks create a self-consistent environment, in which the electric potential in overlapped EDL is determined by both the externally applied potential and the number of ions for screening, allowing migration, diffusion, and steric flux in the same direction. The ions accumulated in overlapped EDL then lead to a nonlinear voltage-current relation indescribable by the Ohmic law with a conventional constant resistance. A dynamically varying trans-slit ionic resistance, as well as its mathematical expression, is identified by machine learning, allowing for construction of a nano-circuitry model (NCM). NCM can rapidly evaluate the collective impact of nanoscopic confinement on the macroscopic performance of supercapacitors, and simultaneously retaining nanometre-resolved ionic behaviour. Here we demonstrate, in an example study of nanoconfined charging dynamics, that the dynamically varying trans-slit resistance could deliver more ions for storage and thus, induces an asymmetric CV and increases the performance. This analysis by NCM is completed within minutes using a laptop computer, in comparison with

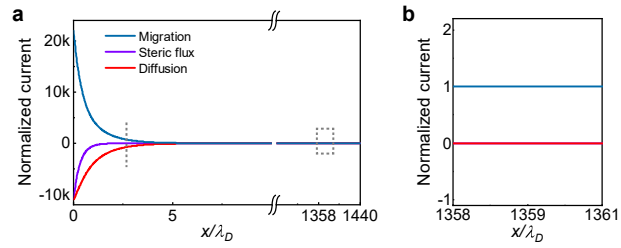
weeks of calculation by mPNP. The result re-emphasizes that charging process of supercapacitors is a balance between ion transport and storage, rather than only depending on the local capacitance of nanoslit. The asymmetric CV further shows a trapezoid shape or a Faradaic-like peak, which are frequently observed in experiments, depending on the nanoconfinement condition. The nanoconfinement condition can be regulated by the interlayer distance, ionic species, electrolyte concentration, and voltage window. While conventional interpretation for the trapezoid shape and the peak involves desolvation and Faradaic processes, our analysis provides an additional perspective of the nanoconfinement-induced dynamically varying trans-slit resistance. Note that the varying resistance could result in a varying charging time constant, which may assist future studies of material microstructure characterization by time constant distribution investigation(50). In future, the demonstrated use of machine learning in this work may be used to analyse other nanoscopic ionic behaviour mathematically, such as solvation-involved intercalation or ion-ion correlation, in pseudo-capacitors, batteries, or desalination, in order to obtain a multiscale description(51–55). This paves the way towards rational design of electrochemical systems.

1. Crabtree G, Rubloff G, Takeuchi E (2017) Basic research needs for next generation electrical energy storage. (Department of Energy), Report.
2. Forse AC, et al. (2015) Nmr study of ion dynamics and charge storage in ionic liquid supercapacitors. *Journal of the American Chemical Society* 137(22):7231–7242.
3. Biesheuvel PM, Bazant MZ (2010) Nonlinear dynamics of capacitive charging and desalination by porous electrodes. *Physical Review E* 81(3):031502.
4. Merlet C, et al. (2012) On the molecular origin of supercapacitance in nanoporous carbon electrodes. *Nature Materials* 11(4):306–310.
5. Kondrat S, Wu P, Qiao R, Kornyshev AA (2014) Accelerating charging dynamics in subnanometre pores. *Nature Materials* 13(4):387–393.
6. Forse AC, Merlet C, Griffin JM, Grey CP (2016) New perspectives on the charging mechanisms of supercapacitors. *Journal of the American Chemical Society* 138(18):5731–5744.
7. Conway B (1999) *Electrochemical Supercapacitors: Scientific Fundamentals and Technological Applications*. (Springer, New York).
8. Zhan H, et al. (2020) Solvation-involved nanoionics: new opportunities from 2D nanomaterial laminar membranes. *Advanced Materials* 32(18):1904562.
9. Simon P, Gogotsi Y (2008) Materials for electrochemical capacitors. *Nature Materials* 7(11):845–854.
10. Sparreboom W, van den Berg A, Eijkel JCT (2009) Principles and applications of nanofluidic transport. *Nature Nanotechnology* 4(11):713–720.
11. Xiao J, et al. (2020) Electrolyte gating in graphene-based supercapacitors and its use for probing nanoconfined charging dynamics. *Nature Nanotechnology* 15(8):683–689.
12. Péan C, et al. (2014) On the dynamics of charging in nanoporous carbon-based supercapacitors. *ACS Nano* 8(2):1576–1583.
13. Bi S, et al. (2020) Molecular understanding of charge storage and charging dynamics in supercapacitors with mof electrodes and ionic liquid electrolytes. *Nature Materials* 19(5):552–558.
14. Mirzadeh M, Gibou F, Squires TM (2014) Enhanced charging kinetics of porous electrodes: surface conduction as a short-circuit mechanism. *Physical Review Letters* 113(9):097701.
15. Lian C, Janssen M, Liu H, van Rooij R (2020) Blessing and curse: how a supercapacitor's large capacitance causes its slow charging. *Physical Review Letters* 124(7):076001.
16. Ngandjong AC, et al. (2017) Multiscale simulation platform linking lithium ion battery electrode fabrication process with performance at the cell level. *The Journal of Physical Chemistry Letters* 8(23):5966–5972.
17. de Levie R (1963) On porous electrodes in electrolyte solutions: I. capacitance effects. *Electrochimica Acta* 8(10):751–780.
18. Wu P, Huang J, Meunier V, Sumpter BG, Qiao R (2011) Complex capacitance scaling in ionic liquids-filled nanopores. *ACS Nano* 5(11):9044–9051.
19. Pilon L, Wang H, d'Entremont A (2015) Recent advances in continuum modeling of interfacial and transport phenomena in electric double layer capacitors. *Journal of The Electrochemical Society* 162(5):A5158–A5178.
20. Jordan MI, Mitchell TM (2015) Machine learning: Trends, perspectives, and prospects. *Science* 349(6245):255.
21. Raccuglia P, et al. (2016) Machine-learning-assisted materials discovery using failed experiments. *Nature* 533:73.
22. Molesky S, et al. (2018) Inverse design in nanophotonics. *Nature Photonics* 12(11):659–670.
23. Farsi H, Gobal F (2007) Artificial neural network simulator for supercapacitor performance prediction. *Computational Materials Science* 39(3):678–683.
24. Akbari E, Mir M, Vasiljeva MV, Alizadeh A, Nilashi M (2019) A computational model of neural learning to predict graphene based ISFET. *Journal of Electronic Materials* 48(7):4647–4652.
25. Schmidt M, Lipson H (2009) Distilling free-form natural laws from experimental data. *Science* 324(5923):81.
26. Brunton SL, Proctor JL, Kutz JN (2016) Discovering governing equations from data by sparse

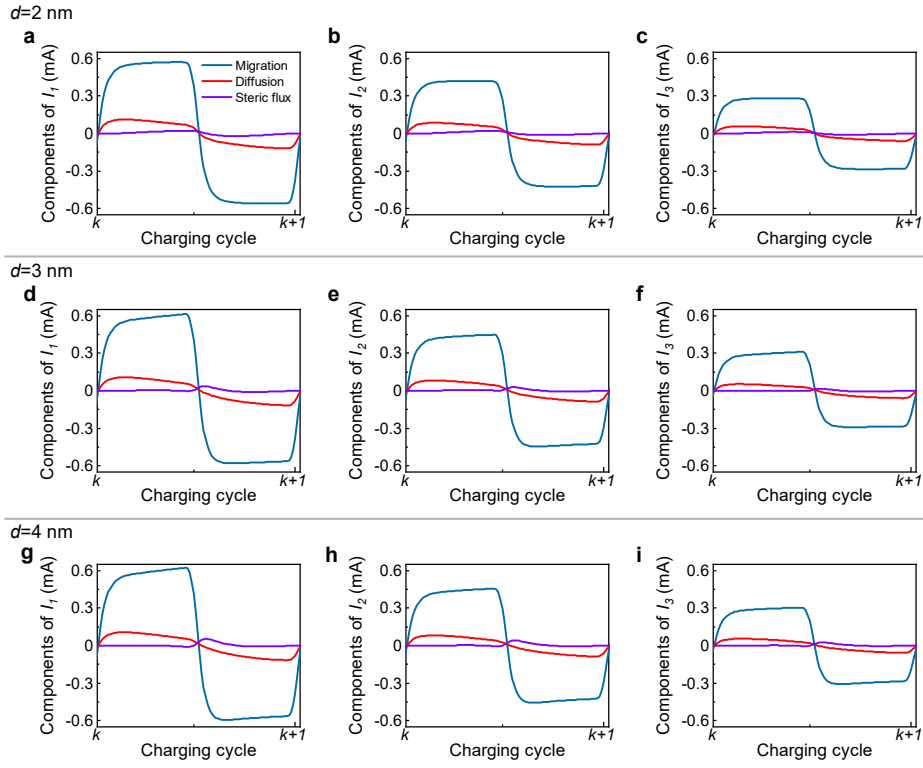
- identification of nonlinear dynamical systems. *Proceedings of the National Academy of Sciences* 113(15):3932.
27. Zhao H, Storey BD, Braatz RD, Bazant MZ (2020) Learning the physics of pattern formation from images. *Physical Review Letters* 124(6):060201.
28. Schoepplein M, Weatheritt J, Sandberg R, Talei M, Klein M (2018) Application of an evolutionary algorithm to les modelling of turbulent transport in premixed flames. *Journal of Computational Physics* 374:1166–1179.
29. Kilic MS, Bazant MZ, Ajdari A (2007) Steric effects in the dynamics of electrolytes at large applied voltages. ii. modified poisson-nernst-planck equations. *Physical Review E* 75:021503.
30. Daiguji H, Yang P, Majumdar A (2004) Ion transport in nanofluidic channels. *Nano Letters* 4(1):137–142.
31. Bazant MZ, Thornton K, Ajdari A (2004) Diffuse-charge dynamics in electrochemical systems. *Physical Review E* 70(2):021506.
32. Zhan H, Hu C (2011) Kinetic solutions for electrons in multi-cusp ion source. *Applied Physics Letters* 99(22):221501.
33. Zhan H, et al. (2011) Theoretical discussion for electron-density distribution in multicusp ion source. *Applied Physics Letters* 98(12):121501.
34. Yang X, Cheng C, Wang Y, Qiu L, Li D (2013) Liquid-mediated dense integration of graphene materials for compact capacitive energy storage. *Science* 341(6145):534–537.
35. Bard AJ, Faulkner LR (2000) *Electrochemical Methods: Fundamentals and Applications*. (John Wiley & Sons, New York, USA).
36. Zhan H, Cervenka J, Prawer S, Garrett DJ (2017) Electrical double layer at various electrode potentials: a modification by vibration. *The Journal of Physical Chemistry C* 121(8):4760–4764.
37. Zhan H (2020) *Graphene-Electrolyte Interfaces: Electronic Properties and Applications*. (Jenny Stanford Publishing, Singapore).
38. Weatheritt J, Sandberg R (2016) A novel evolutionary algorithm applied to algebraic modifications of the stress-strain relationship. *Journal of Computational Physics* 325:22–37.
39. Macdonald JR (1990) Impedance spectroscopy: old problems and new developments. *Electrochimica Acta* 35(10):1483–1492.
40. Zhan H, et al. (2016) Direct fabrication of 3D graphene on nanoporous anodic alumina by plasma-enhanced chemical vapor deposition. *Scientific Reports* 6:19822.
41. Conway BE, Pell WG (2002) Power limitations of supercapacitor operation associated with resistance and capacitance distribution in porous electrode devices. *Journal of Power Sources* 105(2):169–81.
42. Eikerling M, Kornyshev AA, Lust E (2005) Optimized structure of nanoporous carbon-based double-layer capacitors. *Journal of The Electrochemical Society* 152(1):E24–E33.
43. Spyker RL, Nelms RM (2000) Analysis of double-layer capacitors supplying constant power loads. *IEEE Transactions on Aerospace and Electronic Systems* 36(4):1439–1443.
44. Shin D, et al. (year?) Battery-supercapacitor hybrid system for high-rate pulsed load applications in 2011 *Design, Automation & Test in Europe*. pp. 1–4.
45. Zhang S, Pan N (2015) Supercapacitors performance evaluation. *Advanced Energy Materials* 5(6):1401401.
46. Lin R, et al. (2009) Microelectrode study of pore size, ion size, and solvent effects on the charge/discharge behavior of microporous carbons for electrical double-layer capacitors. *Journal of the Electrochemical Society* 156(1):A7–A12.
47. Sun G, et al. (2011) Capacitive matching of pore size and ion size in the negative and positive electrodes for supercapacitors. *Electrochimica Acta* 56(25):9248–9256.
48. Zhu Y, et al. (2011) Carbon-based supercapacitors produced by activation of graphene. *Science* 332(6037):1537–1541.
49. Lukatskaya MR, et al. (2013) Cation intercalation and high volumetric capacitance of two-dimensional titanium carbide. *Science* 341(6153):1502.
50. Song J, Bazant MZ (2018) Electrochemical impedance imaging via the distribution of diffusion times. *Physical Review Letters* 120(11):116001.
51. Qian X, et al. (2020) Beneficial restacking of 2d nanomaterials for electrocatalysis: a case of mos2 membranes. *Chemical Communications* 56(51):7005–7008.
52. Rifai A, et al. (2018) Polycrystalline diamond coating of additively manufactured titanium for biomedical applications. *ACS Applied Materials & Interfaces* 10(10):8474–8484.
53. Zhan H, Cervenka J, Prawer S, Garrett DJ (2018) Molecular detection by liquid gated Hall effect measurements of graphene. *Nanoscale* 10(3):930–935.
54. Yu P, et al. (2019) Electrochemically-derived graphene oxide membranes with high stability and superior ionic sieving. *Chemical Communications* 55(28):4075–4078.
55. Apollo NV, et al. (2018) Cooling of miniature electronic systems using diamond circuit boards in 2018 17th IEEE Intersociety Conference on Thermal and Thermomechanical Phenomena in Electronic Systems (ITherm). pp. 340–344.
56. Cheng C, et al. (2016) Ion transport in complex layered graphene-based membranes with tuneable interlayer spacing. *Science Advances* 2(2):e1501272.
57. Kontturi K, Murtomäki L, Manzanares J (2008) *Ionic Transport Processes: in Electrochemistry and Membrane Science*. (Oxford University Press, Oxford).
58. Feinauer J, et al. (2019) Multibat: Unified workflow for fast electrochemical 3d simulations of lithium-ion cells combining virtual stochastic microstructures, electrochemical degradation models and model order reduction. *Journal of Computational Science* 31:172–184.



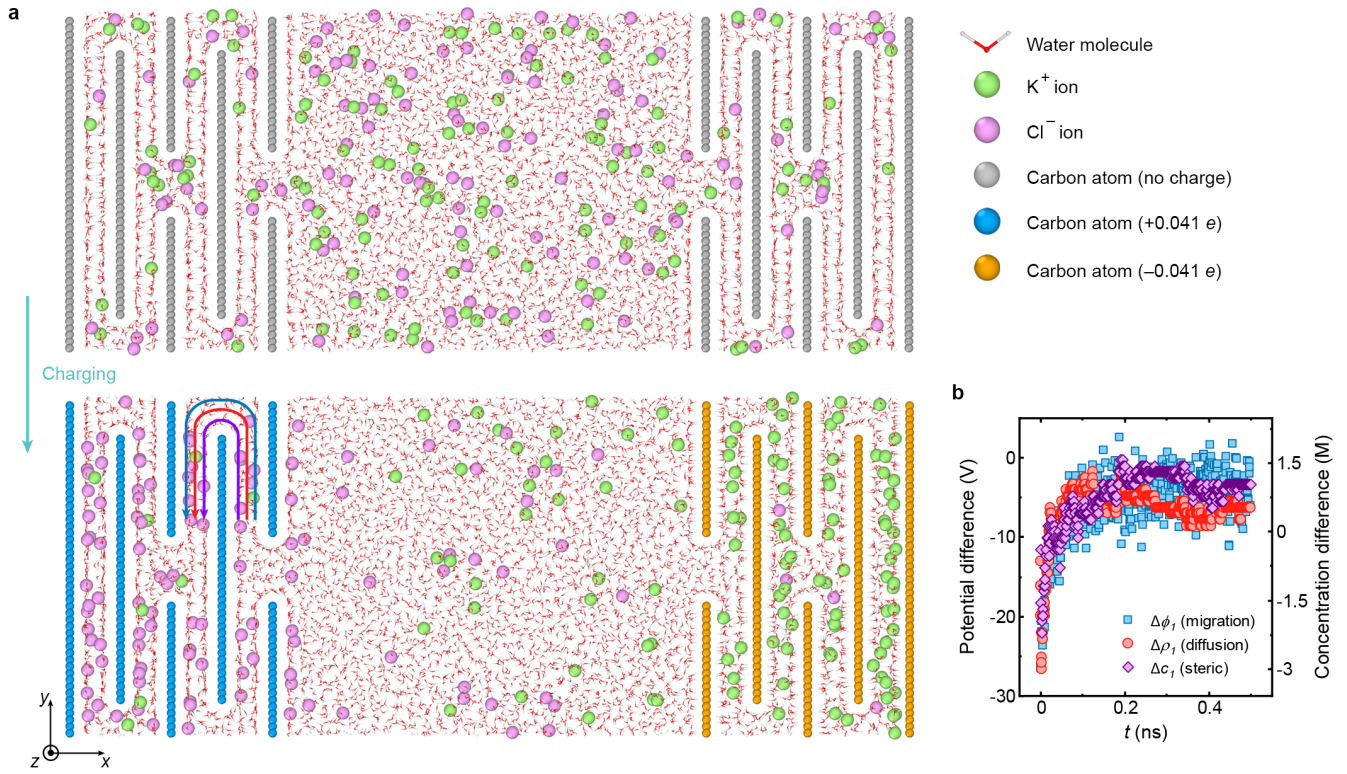
Extended Data Fig. 1. Half-cell model of a membrane-based supercapacitor to investigate charging dynamics using modified Poisson-Nernst-Planck theory. The membrane electrode is comprised of several monolayer 2D materials (orange slats). It follows the statistical representative microstructure model that consists of regularly distributed 2D material layers(56). Each pair of two adjacent 2D materials construct a nanoslit, with i as the index. The top and bottom edges (y -axis) are the mirror planes. The dark cyan region represents the electrolyte filled in the porous electrode and in the open space (reservoir). The contact of electrolyte with each 2D material prior to the application of voltage is to reflect an experimental practice where electrodes are immersed in electrolyte for sufficient time before electrochemical measurements. The rightmost side on x -axis of the half-cell also represents the mid-plane in an equivalent full-cell model. The light cyan regions surrounding each 2D material indicate the Stern layer. Taking advantage of the symmetry of the adopted electrode structure, we only need to simulate the ion transport and storage in this depicted region by using appropriate boundary condition (e.g., vertical flux equals to zero at the top and bottom edges). See Methods for details of our simulations.



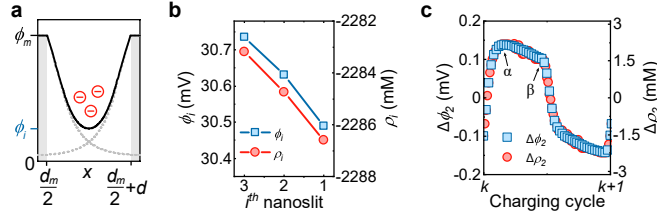
Extended Data Fig. 2. Ion migration, diffusion, and steric flux as a function of distance (x) from the electrode surface in open space. **a**, Normalized current components (migration, diffusion, and steric flux) as a function of normalized distance in open space (Fig. 2b), calculated using the mPNP theory at the instant where the cycle number is around $k + 0.25$. The current components are normalized by the total current in supercapacitor, obtained at the rightmost side of the half-cell model. x is normalized by the Debye length (λ_D), which is around 0.3 nm for 1 M aqueous KCl solution. The dashed vertical line roughly indicates the location where current values in Fig. 2c are reported. **b**, Magnification of the dashed box in (a). The current in the open space (or the bulk electrolyte) is mainly migration. The steric flux is overlapped by diffusion, and they are all negligible here.



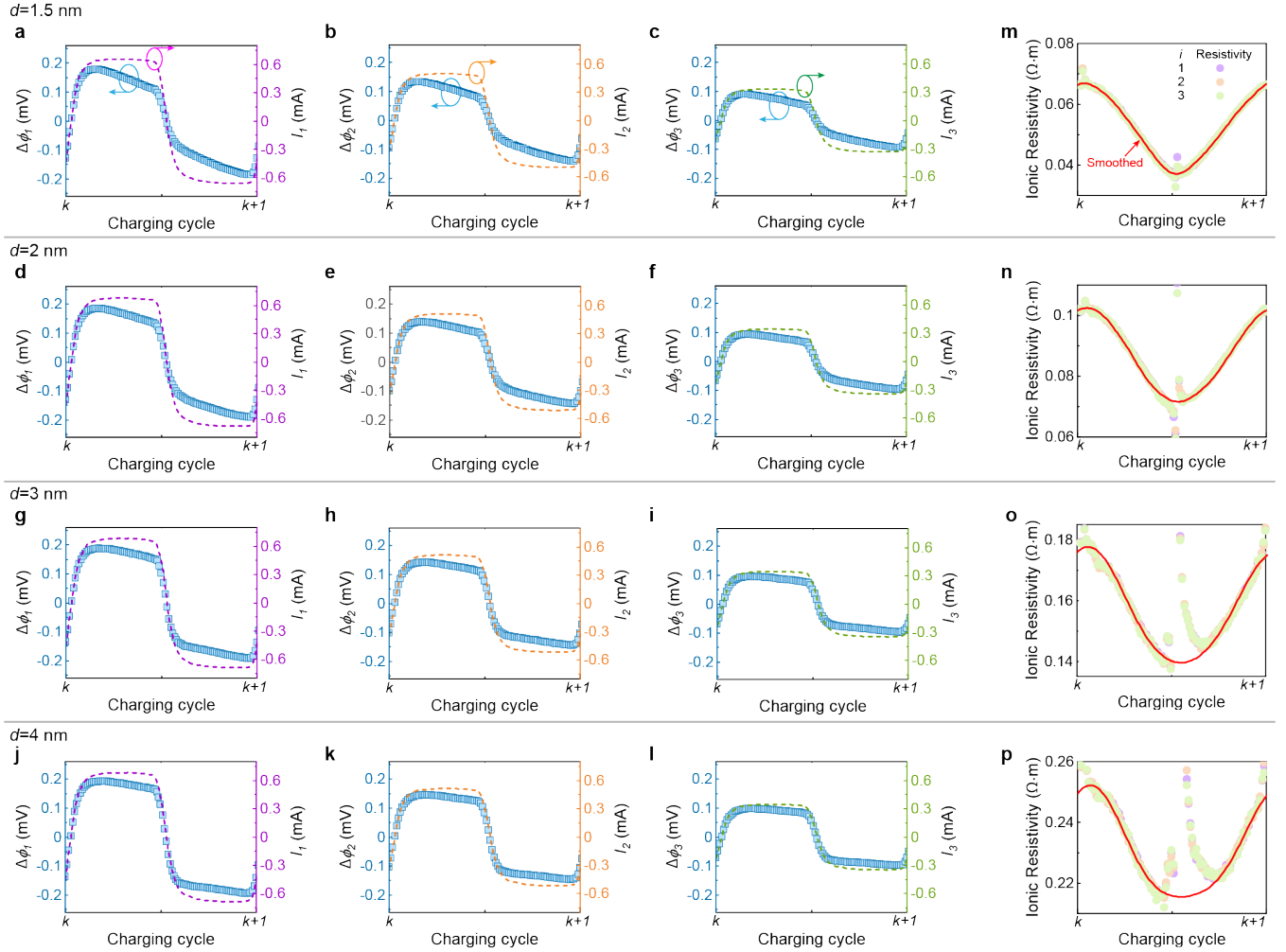
Extended Data Fig. 3. Trans-slit migration, diffusion, and steric flux of ions under nanoconfinement. The variation of trans-slit ionic current (I_i) between the i^{th} and $(i + 1)^{th}$ nanoslits (Fig. 2e) during k^{th} cyclic voltammetry charging/discharging cycle is decomposed into the components of ion migration, diffusion, and steric flux. **a-c**, The slit size (d) or interlayer distance of 2D materials is 2 nm. i is 1 (**a**), 2 (**b**), and 3 (**c**), respectively. **d-f**, $d = 3$ nm. **g-i**, $d = 4$ nm. The scale of I_i in all panels are set the same for comparison. The direction of diffusion is the same as that of migration, leading to the observed diffusion-enhanced migration (Fig. 2e-g). Note that the direction of steric flux tends to become the same as d decreases.



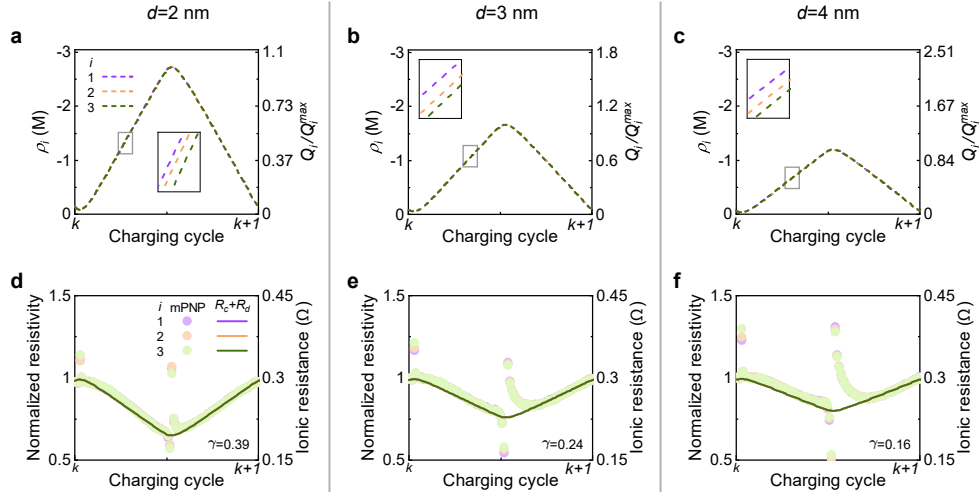
Extended Data Fig. 4. Molecular dynamics studies of trans-slit ion migration, diffusion, and steric flux in a graphene membrane-based supercapacitor during charging process. **a**, Atomic structure of the supercapacitor (details in Methods). Top panel denotes the uncharged case where all carbon atoms possess zero charge. Bottom panel represents the charged supercapacitor, where each carbon atom in left/right electrode possesses a charge of $+0.041e/-0.041e$, respectively. Here e is the elementary charge. For the feasibility of molecular dynamics simulations to investigate the complex charging dynamics, we adopted the fixed charge method (instead of the constant potential method) and applied the charges on carbon atoms suddenly and hold thereafter in a step-function fashion (instead of the gradual charge increase/decrease in experiments and our PNP simulations). The directions of trans-slit ion migration, diffusion, and steric fluxes are illustrated by blue, red, and purple arrows, respectively (see following for details). **b**, The differences of electrical potential ($\Delta\phi_1$, squares), net ion concentration ($\Delta\rho_1$, circles), and total ion density (Δc_1 , diamonds) between the first and second slit as a function of time. The differences follow the same variation trend, which is qualitatively consistent with the results by mPNP simulations. Particularly, the same variation trends of $\Delta\phi_1$ and $\Delta\rho_1$ suggest same direction of migration flux and diffusion flux, due to a strong correlation between charge and electrical potential (see discussion in Extended Data Fig. 5), confirming the observed diffusion-enhanced migration in our mPNP simulations.



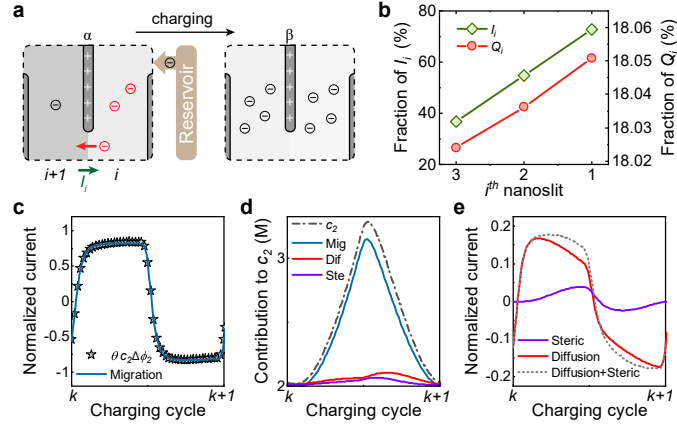
Extended Data Fig. 5. Electric potential and net ion concentration inside nanoslits of membrane-based supercapacitors. **a**, Electric potential well (solid black curve) along x -direction inside the i^{th} nanoslit, calculated by mPNP at $y = 0$ in Fig. 2e. The shaded regions indicate two 2D material sheets used to construct the boundaries/walls of the nanoslit, which have an identical positive surface potential ϕ_m in this case. The counter-ions in nanoslit must screen ϕ_m from both sheets, while in open space they only screen ϕ_m from one electrode surface by forming an EDL (Fig. 2d). Therefore, the potential well in nanoslit is contributed the overlap of two EDLs from each of the 2D material sheets (dotted grey curves). **b**, ϕ_i and the net ion concentration (ρ_i) in three adjacent nanoslits in a nanoslit network at the instant where the cycle number is around $k + 0.25$. Here $d = 2$ nm. It is clear that a more negative value of ρ_i corresponds to a lower ϕ_i . This is reasonable because according to the sketch in (a), a higher anion concentration gives rise to better screening of positive ϕ_m and thus a smaller ϕ_i . **c**, The trans-slit voltage (or potential difference, $\Delta\phi_2 = \phi_3 - \phi_2$) and net ion concentration difference ($\Delta\rho_2 = \rho_3 - \rho_2$) between the 3rd and 2nd nanoslit during a typical charging/discharging cycle. The observed strong correlation confirms that the observation in (b) persists during the whole charging cycle. Therefore, we can understand why the ion migration (driven by $\Delta\phi$) and net ion diffusion (driven by $\Delta\rho$) have the same direction (Fig. 2 and Extended Data Fig. 3). Note that the trans-slit voltage decreases after reaching the maximum at point α (see discussion in Extended Data Fig. 8).



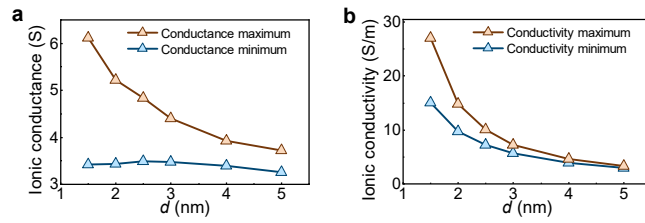
Extended Data Fig. 6. Trans-slit voltage ($\Delta\phi_i$), current (I_i), and the directly derived dynamically varying ionic resistivity during a typical charging/discharging cycle. a-l, $\Delta\phi_i$ (blue squares) and I_i (dashed lines) between the i^{th} and $(i+1)^{th}$ nanoslit in membranes with slit height $d = 1.5$ (a-c), 2 (d-f), 3 (g-i), and 4 nm (j-l), respectively. The index i of a nanoslit indicates its location in x -axis in the supercapacitor electrode (Extended Data Fig. 1). The trans-slit ionic resistivity derived directly using $\Delta\phi_i$ and ΔI_i , and it is studied here for comparison for intrinsic ion transport in nanoslits with different heights. The significant variation of ionic resistivity during a charging cycle clearly indicates its dynamic feature. m-p, The resistivity remains identical for different nanoslits in the same membrane, although both $\Delta\phi_i$ and I_i decrease with the increasing i . This observation is valid for different values of d . Overall, we can draw three conclusions regarding dynamic ion resistivity. First, in a membrane electrode with a given slit size, the dynamic ion resistivity value is independent of the slit location. Second, the magnitude of dynamic resistivity increases as slit size d increases, which is counter-intuitive (see main text for discussion). Third, the difference between the maximum and minimum of the dynamic ionic resistivity (variation magnitude) seems unchanged (or only slightly increased) with the increasing d , which is summarized in Fig. 3d. As such, the difference between the maximum and minimum resistance is larger in small slit size, which can also be inferred from the dependence of deviation between $\Delta\phi_i$ and I_i during charging/discharging on d . This indicates that the effect of dynamic variation of ionic resistance becomes more profound as d decreases (Fig. 3c and Extended Data Fig. 9).



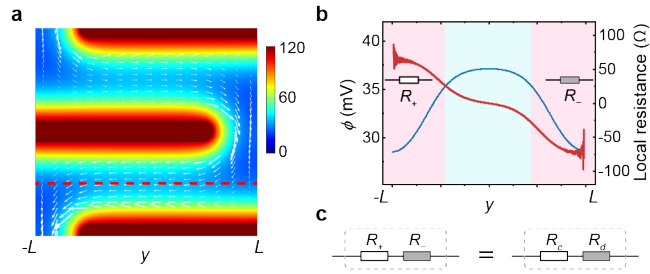
Extended Data Fig. 7. Net ion storage in i^{th} nanoslit and the trans-slit resistivity and resistance. **a-c**, Net ion storage in the i^{th} nanoslit of a membrane electrode [ρ_i : concentration, Q_i/Q_i^{max} : normalized storage used in equation 1b], where the slit size d is 2 **(a)**, 3 **(b)**, and 4 nm **(c)**, respectively. The insets are the magnification of the lines in the grey boxes, showing that $\rho_i > \rho_{i+1}$. The slight difference of ρ_i among nanoslits are responsible for the trans-slit voltage $\Delta\phi_i$, due to the charge-potential correlation (Extended Data Fig. 5). **d-f**, Trans-slit resistivity (normalized with respect to its maximum) and resistance described by net ion storage through equation 1b ($R_c + R_d$, solid lines), which is consistent with that directly obtained from the voltage-current relation in mPNP simulation (filled circles, same as that in Extended Data Fig. 6h, l, p). d is 2 **(d)**, 3 **(e)**, and 4 nm **(f)**. As we are interested in understanding the effect of intrinsic ion properties (e.g., ρ_i) on geometry-related quantities (e.g., resistance) in nanoslits, the relative change in resistivity is discussed. (1), In nanoscopic level, ions accumulate in nanoslits and increase ρ_i during charging, leading to the dynamically varying trans-slit resistivity. (2), In terms of the nano-macro translation, ρ_i is a quantity also available in macroscopic models allowing for the description of resistivity, while the conventional definition of resistivity involves the total ion concentration (c_i) which is only available in nanoscale. (3), In macroscopic level, $R_c + R_d$ automatically includes the contribution of migration, diffusion, and steric flux, while the nanoscopic quantity c_i is only able to account for migration (Extended Data Fig. 8c). Note that the small difference in ρ_i results in nearly identical resistivity for different i . Also note that the difference between the maximum and minimum of resistivity decreases as d increases. This is because ion accumulation in ρ_i becomes more notable as d decreases where EDL overlaps substantially. This indicates that the dynamically varying resistivity, although with an unchanged absolute difference (Δr in Fig. 3d), has a relatively smaller overall effect with larger d .



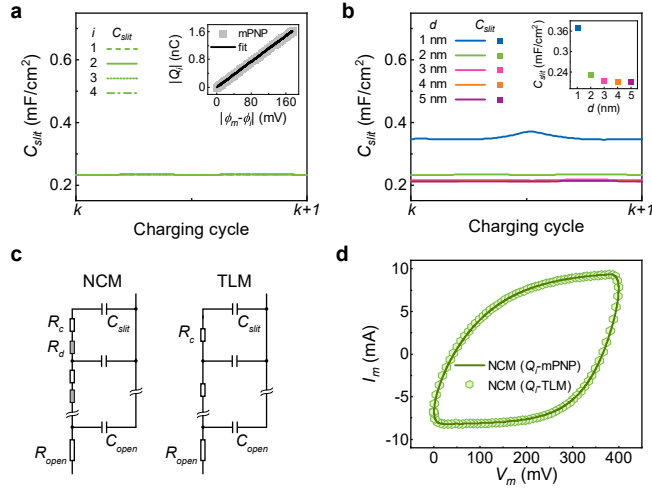
Extended Data Fig. 8. Trans-slit current of nanoconfined ions: impact on trans-slit voltage and its origin from diffusion-assisted migration. **a**, Variation of the net ions and electrical potential (indicated by grayscale) in the i^{th} and $(i+1)^{\text{th}}$ nanoslits, as ions are carried by the trans-slit current (I_i , green arrow) during a charging process at the time points α and β in Extended Data Fig. 5c. The sign of the net ion is negative here due to the positive potential on 2D material. Note that the direction of I_i is opposite to the flow of net ions (red arrow) due to the negative sign. **b**, Calculated fractions of I_i (green diamonds) and net ions (Q_i , purple circles) in three neighbouring nanoslits at the point α , with respect to Q_m and I_m . $Q_i = \int \rho_i dV_i$, where V_i is the volume of the i^{th} nanoslit. $Q_m = \sum_i Q_i$ represent the net ions stored in the entire membrane electrode, and I_m is the total current in the circuit. Note that Q_m cancels the negative sign of Q_i in the fraction. Before the point α is reached during charging, $\Delta \phi_i$ and $\Delta \rho_i$ in Extended Data Fig. 5c increase because anions from the bulk electrolyte always reach the i^{th} nanoslit before the $(i+1)^{\text{th}}$, i.e., a higher fraction of Q_i than Q_{i+1} . The higher fraction of Q_i continuously moves/supplies the ions from the i^{th} nanoslit to the $(i+1)^{\text{th}}$ through the current I_i . Note that $I_i > I_{i+1}$, because when ions are travelled to the $(i+1)^{\text{th}}$ nanoslit, some ions are stored/left and less ions keep travelling to the $(i+2)^{\text{th}}$ nanoslit. As charging proceeds beyond α , this ion supply process decrease the difference between Q_i and Q_{i+1} , i.e., accounting for the observed decrease in $\Delta \phi_i$ and $\Delta \rho_i$ in Extended Data Fig. 5c. **c**, Quantitative description of migration by $\Delta \phi_2$ and the total ion concentration (c_2), accounting for the nonlinear relation between the trans-slit voltage and migration only. θ is a constant analogous to mobility. **d**, Contribution to the accumulation of c_2 (dash-dotted curve) from migration (blue), diffusion (red) and steric flux (violet) during a charging cycle. **e**, Diffusion current compensated by steric flux, further contributing to the nonlinearity between the trans-slit voltage and current.



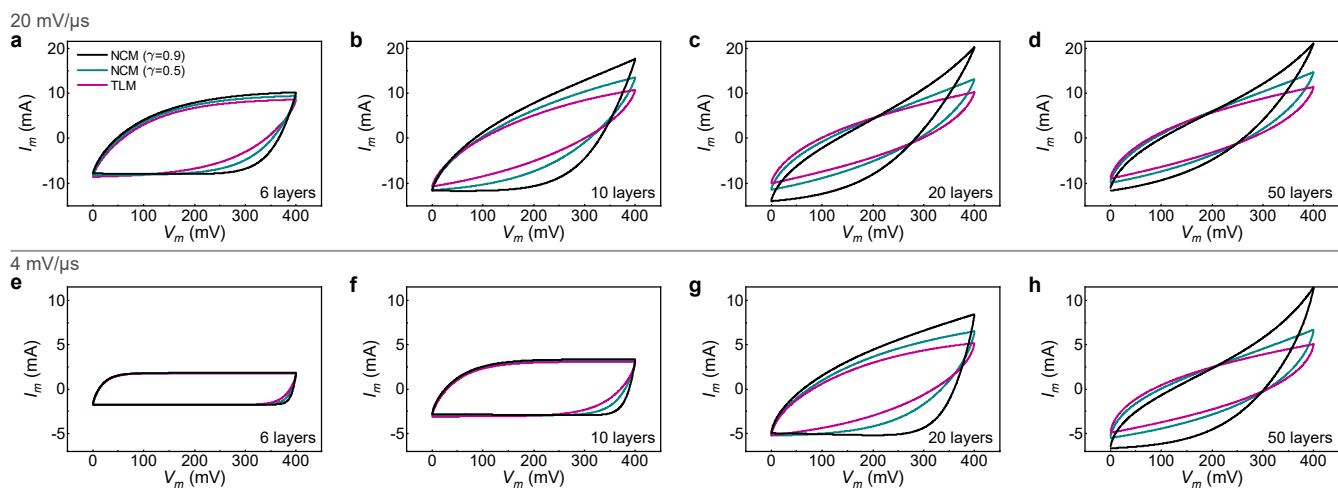
Extended Data Fig. 9. Trans-slit conductance and conductivity as a function of the slit size (d). **a**, The conductance at the beginning of charging has the minimum value (blue triangles), and it is nearly constant in spite of different values of d . When d decreases, only the space between 2D materials (dark slats in Fig. 2b) is reduced; the interfacial area between the 2D materials and nanoconfined electrolyte remains unchanged. This suggests that the conduction is most likely relevant to the ions in the interface, i.e., surface-conduction. **b**, The conductivity is the inverse of the resistivity in Fig. 3d. The difference between the conductivity maximum and minimum reaches increases when d decreases while Δr in Fig. 3d remains nearly unchanged, confirming that the nonlinear voltage-current relation, although exists in nanoslits with all sizes, dominates as d decreases.



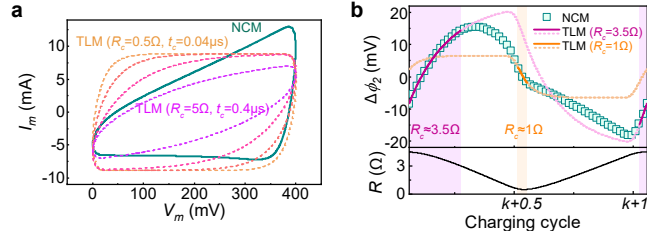
Extended Data Fig. 10. Spatial investigation of the local potential and current in nanoscopic simulation for the study of resistance distribution in macroscale. a, Spatial investigation of potential (colour-scale unit: mV) and current (arrows) in nanoslits by mPNP at a time point during the charging process. The potential applied on 2D materials has not reached its maximum (200 mV) yet. $d = 1.5$ nm here. The length of the white arrows indicates the magnitude of the local current density or ion flux. Note that the arrows for ion flux across two nanoslits are clearly longer located near the material surface than those at $y = \pm L$. **b,** Electrical potential (ϕ , blue line) and the derived local resistance (red line) and along the violet dashed line in (a). The local resistance clearly has large positive (R_+) and negative (R_-) values in the pink region, while in the cyan region the local resistance is very small. R_+ and R_- result from the sharp slope of ϕ with opposite values in the left and right red regime, due to ion accumulation in overlapped EDL, with a unidirectional current. Note that, although this spatial investigation is only analysed from a snapshot, R_+ and R_- should be time-dependent. **c,** A schematic diagram showing that the effect of serial connected R_+ and R_- on trans-slit ion transport is equivalent to the sum of R_c and R_d .



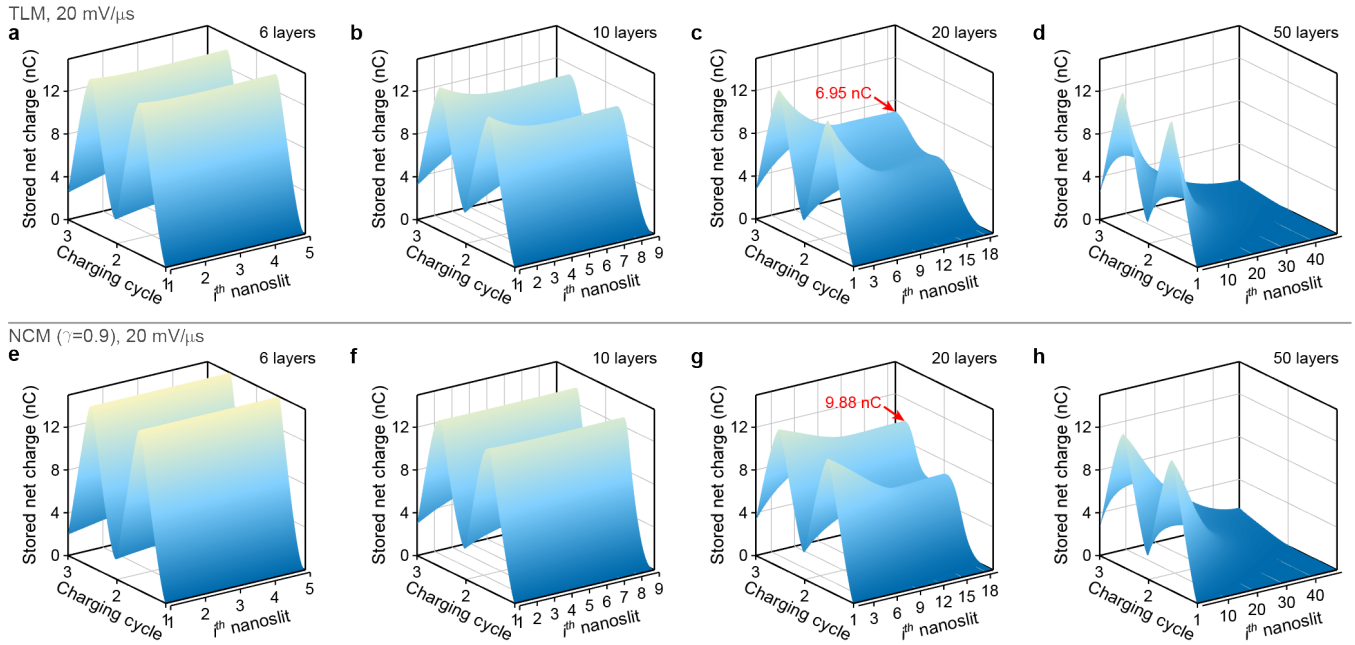
Extended Data Fig. 11. Nanoscopic capacitance of nanoslits and the construction of macroscopic equivalent circuits. **a**, Nanoscopic capacitance (C_{slit}) of different nanoslits (represented by i) in the same membrane as a function of time, which all coincide with each other. The slit size d is 2 nm. Inset: linear fit of the stored charge ($|Q_i|$) vs. the voltage ($|\phi_m - \phi_i|$) in a nanoslit. This shows that C_{slit} is constant in space and time. **b**, C_{slit} of the 2^{nd} nanoslit as a function of time, where d changes from 1 to 5 nm. When $d > 1$ nm, C_{slit} is a constant over the charging cycle. Inset: C_{slit} in the middle of the charging cycle as a function of d . **c**, Nano-circuitry model (NCM, left) and transmission line model (TLM, right) for the half-cell of a supercapacitor. **d**, CV diagrams by NCM for a membrane-based supercapacitor consisting of 6 layers of 2D materials with $d = 1.5$ nm. The variation of V_m is smoothed here (bottom panel in Fig. 2c). Note that, in order to calculate R_d conveniently for NCM, Q_i used in equation 1b could be obtained from mPNP (solid line) or approximated by TLM (hexagon), where the resultant CV diagrams are identical here.



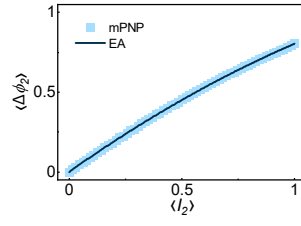
Extended Data Fig. 12. Impact of nanoconfined ions on the macroscopic performance of supercapacitors, described by the nano-circuitry model (NCM) and the transmission line model (TLM). The supercapacitors are operated at the charging/discharging rates of $20 \text{ mV}/\mu\text{s}$ (**a-d**) and $4 \text{ mV}/\mu\text{s}$ (**e-h**). The value of resistance and capacitance for each circuit element is obtained from previous mPNP studies where $d = 1.5 \text{ nm}$ and $\gamma = 0.5$. The degree of nanoconfinement effect is weighted by γ in NCM, where $\gamma = 0.9$ indicates severely confined ions in membrane electrodes (see Extended Data Fig. 7 for more discussion of γ). Note that TLM corresponds to the NCM where $\gamma = 0$. The membrane electrodes of the supercapacitors consist of 6 (**a, e**), 10 (**b, f**), 20 (**c, g**), and 50 (**d, h**) layers of 2D materials. The slit size d is 1.5 nm . V_m is not smoothed here, as mPNP simulation is not required. These results give two implications at the macroscopic level. (1), Although the nanoconfined ions may only have little effects in membranes with a few layers of 2D materials (**e, f**), when the number of layer increases, the collective effect of nanoconfined ions increases and it could change the macroscopic behaviour (**g, h**). (2), The difference between (**a, b**) and (**e, f**) implies that the nanoconfinement effect could higher impact when the charging/discharging rate is high.



Extended Data Fig. 13. Dynamically varying ion resistance as the mechanism of the asymmetric CV diagram. Charging process is a balance between ion storage and transport. In addition to the general interest on the capacitance and voltage in EDL for ion storage, the limitation of ion supply by resistive transport across nanoslits must also be noted. **a**, The CV diagrams obtained by TLM (dashed lines) for any values of R_c does not reproduce the asymmetric CV obtained by NCM (dark cyan line), as the TLM-obtained CV is always symmetric. This implies that the nanoscopic ion dynamics described by NCM can be fundamentally different from that described by TLM. Here $R_c = 5\Omega$. The minimum value of $R_c + R_d$ for NCM could reach 0.5Ω . Purple to orange for TLM: R_c changes from 5, 2, 1, to 0.5Ω , with the corresponding charging time constants $t_c = R_c C$ varying from 0.4, 0.16, 0.08, to $0.04\mu s$. Here $C = 0.08\mu F$ is the capacitance of the electrode. **b**, The nanoscopic discussion of ion dynamics in NCM, for the interpretation of the asymmetric CV, could be obtained by the time-dependant trans-slit resistance ($R = R_c + R_d$, bottom panel). There are two perspectives to understand this. (1), Direct discussion of nanoscopic ion transport by R . In nanoslit network, the trans-slit voltage ($\Delta\phi_i$) stimulates ion transport across nanoslits, which can be modulated by R . This modulation changes the trans-slit current which carries ions for storage, and hence changes the total current I_m . Here $i = 2$ is demonstrated. At the beginning of charging, $\Delta\phi_2$ increases rapidly in the positive direction (dark cyan squares in the top panel) to provide enough current for ion storage due to the large resistance (left purple region). As charging proceeds, $\Delta\phi_2$ decreases as the small value of R requires only a low voltage to supply enough ions for storage (orange region). A small $\Delta\phi_2$ would induce a large voltage across C_{slit} in Extended Data Fig. 11c, allowing for storage of more ions. However, as the large R at the beginning of charging limited the storage of ions to a low value, the current must reach a remarkably high value to drastically increase ion storage. At the beginning of discharging, $\Delta\phi_2$ slowly increase in the negative regime to reverse the charging current to discharging current due to the small value of R . At the end of discharging, $\Delta\phi_2$ approaches to a value determined by TLM with large R (right purple region). (2), Another perspective to understand the asymmetric CV diagram is through t_c , which describes the time needed for the charging/discharging current to reach a steady state. The steady state can be described by a constant value of I_m where trans-slit ion transport can steadily supply ions for storage in nanoslits. When $t < t_c$, the resistive trans-slit current provides ions at a low rate to nanoslits for storage, the trans-slit voltage keeps increasing such that ion storage rate increases towards the steady state. However, t_c is not constant in NCM due to the varying trans-slit resistance. As charging proceeds, the current described by NCM increases faster than that defined by TLM with large R due to the decreased t_c . At the beginning of discharging, the current rapidly reaches a “steady state” due to the small t_c . Although t_c further decreases during discharging, the current does not change significantly as TLMs with small R are also approaching the “steady state”.



Extended Data Fig. 14. Nanoscopic evolution of net charge storage in each nanoslit within the membrane electrode of supercapacitors, obtained by transmission line model (a-d, TLM) and nano-circuitry model (e-h, NCM). $\gamma = 0.9$ for NCM here, all conditions are the same as those for Extended Data Fig. 12. The initial two CV charging/discharging cycles are shown. Net charge stored in the nanoslit with high index (i) near the current collector is clearly smaller than that with low index near the bulk electrolyte, primarily due to slow ion transport(3, 57, 58). Here NCM suggests that, due to the decreased trans-slit ionic resistance or enhanced ion transport under nanoconfinement discussed in Extended Data Fig. 13b, the net charge inside the electrode can increase, for example, the charge stored in the 19th layer described by NCM (9.88 nC) is around 42% higher than that described by TLM (6.95 nC). This results in a better charge storage performance demonstrated by the larger area of CV curve by NCM than that by TLM in Extended Data Fig. 12. Note that these results by both circuit models are obtained within a minute using a laptop computer, in comparison with days or weeks of calculation by mPNP.



Extended Data Fig. 15. Identification of the dynamically varying resistance (R_d) by evolutionary algorithm (EA). Identification of R_d from the non-linear relation between the time integral of trans-slit current (I_2) and voltage ($\Delta\phi_2$) in the 2^{nd} nanoslit with $d = 2$ nm. The light blue squares are the data directly obtained from mPNP simulation, while the solid curve, along with its explicit mathematical expression (equation 1b), is discovered by EA. Since the resistance is identical in different nanoslits (Extended Data Fig. 6), the obtained R_d can be used throughout all nanoslits in the membrane electrode.

Extended Data Table 1. Parameters used for the molecular dynamics simulation

Atoms	ϵ (Kcal/mole)	σ (Å)	Charge (e)
H	0.0	2.058	+0.424
O	0.155	3.166	-0.848
K	0.087	3.143	+1.0
Cl	0.15	4.045	-1.5
C	0.068	3.407	0.0 (before charging) $\pm 0.041^*$ (charging)

*Each carbon atom in the left electrode is assigned $+0.041e$, while those in the right $-0.041e$.